Adaptive Finite Element Analysis of Hypersonic Laminar Flows for Aerothermal Load Predictions

R. Ramakrishnan*
Old Dominion University, Norfolk, Virginia 23508
E. A. Thornton†
University of Virginia, Charlottesville, Virginia 22903
and
A. R. Wieting‡
NASA Langley Research Center, Hampton, Virginia 23665

The use of an adaptive mesh refinement procedure for analyzing hypersonic laminar flows with application to aerothermal load predictions is described. The adaptation procedure, which uses both quadrilateral and triangular elements, is implemented with the multistep Galerkin-Runge-Kutta scheme. Elements that lie in regions of strong gradients are refined based on indicators to obtain better definition of flow features. The effectiveness of the adaptive procedure is demonstrated by modeling Mach 11.7 flow over a 15-deg ramp. Numerical results are compared with predictions of strong interaction theories and experimental data. Surface quantities such as heating rates and pressure loads, critical for the effective design of high-speed vehicles, are found to be in good agreement with experimental values.

Nomenclature

A = element area
C = Chapman-Rubesin parameter
C_f = skin friction coefficient
C_H = heat transfer coefficient
C_p = pressure coefficient
$c^1, \ldots, c^4$ = Runge-Kutta constants
$\boldsymbol{D}_2, \boldsymbol{D}_4$ = artificial dissipation fluxes
E_1, E_2 = flux components
e = element error measure
$\boldsymbol{F}^a, \boldsymbol{F}^v, \boldsymbol{F}^h$ = advective, viscous, and heat flux, respectively
G = growth factor
M = Mach number
$[M]$ = mass matrix
$[N]$ = element interpolation function
$\boldsymbol{n}$ = unit vector normal to surface
n_x, n_y = components of unit vector $\boldsymbol{n}$
Pr = Prandtl number
p = pressure
q_n = heat flux normal to surface
R = global nodal residual
Re = Reynolds number
r = coordinate index
S = solution domain boundary
s = coordinate along ramp surface
T = temperature
T_x, T_y = surface tractions
t = time
U = typical conservation variable
u, v = velocity components in coordinate directions
X = interaction parameter
x_1, x_2 = coordinate directions
Y = maximum element error
α = threshold value for refinement
β = threshold value for derefinement and grid stretching parameter
γ = ratio of specific heats
δ_{ij} = Kronecker delta
θ = element refinement indicator
λ_1, λ_2 = components of unit normal vector
ρ = key variable for refinement
τ_w = shearing stress

Subscripts

aw = adiabatic wall
d = dynamic conditions
i = summation index
j = index for nodes
o = total conditions
res = reservoir conditions
w = wall quantities
∞ = freestream conditions

Superscripts

k = index for multistep scheme
n = time step

Received Sept. 26, 1989; revision received May 15, 1990; accepted for publication May 15, 1990.

*Research Associate, Department of Mechanical Engineering and Mechanics. Member AIAA.
†Professor, Department of Mechanical and Aerospace Engineering. Associate Fellow AIAA.
‡Head, Aerothermal Loads Branch, Structural Mechanics Division. Member AIAA.

Introduction

THE potential role of computational fluid dynamics (CFD) in the design and analysis of high-speed vehicles is being clearly defined by the National Aero-Space Plane, which is envisaged to have applications at flight speeds exceeding Mach 25. Computational techniques that provide good understanding of the flow features and accurate estimates of aerothermal loads is essential in the design of such vehicles since ground based facilities cannot simulate the entire flight envelope. Description of the complex inviscid-viscous interactions with vehicle surfaces is possible with the full Navier-Stokes equations. At the Aerothermal Loads Branch at NASA Langley Research Center, finite element methodology is being developed for integrated fluid-thermal-structural analysis, which

can accurately predict the heating rates, pressure loads, and thermal/structural response.

Compressible flows may contain discontinuities such as shocks as well as regions of high gradients such as boundary layers and shear layers, which need to be resolved. Since these flow phenomena occur over small distance scales, which are not known a priori, the computational mesh needs to be adapted to model high-gradient regions without the use of an excessive number of elements in low-gradient regions. Adaptive mesh refinement procedures can be used effectively to resolve details in the flow region and minimize elements elsewhere. Such procedures lead to highly unstructured meshes. Since finite methods are characterized by their ease in handling completely unstructured meshes and their ability to include mesh refinement procedures, these methods are pursued. Finite element schemes have also demonstrated their capacity to produce good results for a variety of flow situations and configurations.[1–4]

Mesh refinement procedures for triangular finite element meshes were initially detailed by Zienkiewicz et al.,[5] and the application of these procedures to steady[6] and transient[7] compressible flow problems has been demonstrated extensively. Adaptive procedures for finite element meshes with quadrilateral elements have been developed by Oden et al.,[8] and a mesh regeneration scheme developed by Peraire et al.[9] has found application in generating meshes comprised of triangles (in two dimensions) and tetrahedrons (in three dimensions) for inviscid flows. Most of the research in adaptive finite element methods has been in inviscid flows. A recent effort using an upwind finite element formulation to model the inviscid and viscous flow features for shock interaction on a cylindrical leading edge is described in Ref. 2.

The purpose of this paper is to describe the application of an adaptive refinement procedure to predict heat transfer and pressure loads for hypersonic laminar flows. The adaptive refinement procedure and finite element formulation used in Ref. 10 are extended to model the compressible Navier-Stokes equations to detail viscous flow features.

Mesh Adaptation

The classical finite element mesh refinement scheme is the addition of elements in regions of high gradients. Elements that lie in these regions are divided into smaller ones by a subdivision process. Both triangular and quadrilateral elements can be enriched by adding a central node and/or midside nodes. For a typical quadrilateral element, such a subdivision can result in the generation of four smaller elements with the possibility of midside nodes not being connected to neighboring elements. These midside nodes are sometimes called hanging nodes. The solution algorithm must be modified to account for hanging nodes, typically by introducing constraint equations. One way to avoid these unconnected nodes and the special constraints is to transition from a crude quad mesh to a fine one using triangular elements. Automation of the adaptive procedure is accomplished with refinement indicators.

Refinement Indicators

The rationale for using refinement indicators is that, although it is possible to predict the location and strength of shocks, boundary layers, etc., for some simple flow situations, the analyst in general will not have prior knowledge of the location of regions containing sharp changes in flow variables. The decision to refine a particular region of the mesh can be based on either a priori or a posteriori error estimates. The procedure adopted in this paper is to refine the mesh at a certain stage in the analysis, the refinement being based on error indicators computed on the initial mesh. The new mesh is used for a subsequent analysis and then further refinements and analyses are performed if needed.

The aim of the adaptive mesh refinement is the minimization of maximum errors that occur in the finite element domain. An optimal mesh satisfies the equal distribution condition that the error measure is uniformly distributed for all elements of the finite element mesh. The adaptive mesh refinement procedure is designed to add elements in appropriate regions to satisfy this condition. Since the solution is not known a priori, an approximation to the error measure is computed using the finite element solution. If ρ is considered the key variable representative of overall solution behavior, then an error measure for refinement is given by

$$e_i = \sum_{j,k=1}^{2} \theta_{jk} \tag{1}$$

where e_i is the element error and θ_{jk} are scaled second derivatives with a typical term θ_{12} defined as

$$\theta_{12} = \theta_{xy}$$

where

$$\theta_{xy} = \frac{\rho_{,\,xy}}{\left|\left\{|\rho_{,\,x}| + \varepsilon \sum_{i=1}^{nd} |\rho_{,\,x}|_i\right\}_{,y}\right|} \tag{2}$$

Here, nd is the number of nodes in element i, and the comma implies partial differentiation. The first term in the denominator of Eq. (2) scales the second derivative of the key variable to ensure that gradients of different strengths are adapted equally. This prevents the strongest shock from being overly refined at the expense of capturing weaker gradients. The coefficient ε in the second term is used as a filter to handle oscillations in the vicinity of shocks.

The procedure adopted in this paper is to refine all elements that satisfy the criterion

$$e_i > \alpha Y \tag{3}$$

and derefine all elements that satisfy

$$e_i < \beta Y \tag{4}$$

where α and β are preset threshold constants and Y the maximum element error over the entire domain. The key variable used for the refinement is typically density and α and β are usually 0.2 and 0.1, respectively.

Adaptive Procedure

The starting point of the adaptive procedure is a skeleton mesh or base mesh that contains only a few elements. Prior to the first analysis, the mesh refinement program does an overall refinement wherein each element of the skeleton mesh is subdivided into four quad elements. This procedure is repeated a few times until the nodal density of the resulting mesh is deemed sufficient to obtain a solution that captures the main details of the flowfield.

Refinement indicators are computed based on the solution obtained on this initial mesh, and elements that need to be refined or derefined are identified. All elements in the mesh that have indicators above the preset refinement threshold value are enriched, whereas those elements that have values below the threshold derefinement value are coarsened. The refinement strategy permits, at each mesh change, only one level of refinement or derefinement. On refinement of a typical element, the subelements that result could be all quads or a combination of quads and triangles. The number and type of the resulting subelements depend on the refinement level of elements that surround this element.

Figure 1 show the elements that result in a typical refinement and coarsening procedure. Fig. 1a shows the original mesh where elements B, C, and D are to be refined. The mesh that results is seen in Fig. 1b. If, on this refined mesh,

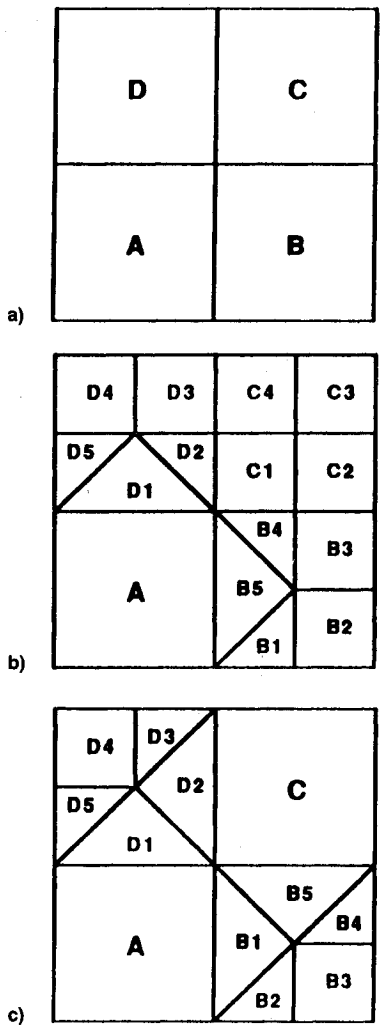

Fig. 1 Example of adaptation procedure using triangular transition elements: a) original mesh; b) refinement of elements B, C, and D; and c) derefinement of element C.

element group C, which includes subelements C1, C2, C3, and C4, needs to be coarsened, the mesh that results after derefinement appears in Fig. 1c.

Boundary-Layer Refinement

In addition to the refinement based on the error indicator detailed in earlier sections, the facility to generate layers of structured quad elements at the wall is also included. This technique is employed to ensure a high density of nodes at no-slip boundaries to resolve thin laminar hypersonic boundary layers. Elements located at the wall are divided into a specified number of subelements; these subelements can be refined and coarsened at successive refinement levels. The nodal coordinates of these new elements are defined such that the mesh generated is stretched normal to the wall. The location of the nodes along normal lines at each wall location is obtained from the expression of Roberts,[11]

$$\delta_i = \frac{[(\beta + 1) - (\beta - 1)/\phi]}{\phi + 1} \qquad 1 < \beta < \infty$$

with

$$\phi = \left[\frac{(\beta + 1)}{(\beta - 1)}\right]^{1-r}$$

$$x_j = x_w + \Delta x \delta_i \tag{5a}$$

$$y_j = y_w + \Delta y \delta_i \qquad j = 1, n\text{new} \tag{5b}$$

where $n$new is the number of new elements that result from the subdivision, Δx and Δy the grid spacings in the coordinate directions, β the grid stretching parameter, and r the coordinate index given by,

$$r = \frac{j}{n\text{new}} \tag{6}$$

where j is the index locating the node from the wall in the normal direction. The nodal unknowns for the new grid points at each wall location are linearly interpolated from the nodal values of the parent element. The meshing procedure clusters more nodes near the wall as the stretching parameter β approaches unity.

Finite Element Formulation

The explicit multistep Galerkin-Runge-Kutta formulation used in Ref. 10 for inviscid flow is extended to model the compressible Navier-Stokes equations. The solution algorithm is applied to the flow equations in conservation form

$$\boldsymbol{U}_{,t} + \boldsymbol{E}_{i,i} = 0 \tag{7}$$

where $\boldsymbol{U}$ is the vector of variables and $\boldsymbol{E}_i$ the flux vectors. The flux vectors are written as

$$\boldsymbol{E}_i = \boldsymbol{F}_i^a - \boldsymbol{F}_i^v - \boldsymbol{F}_i^h \tag{8}$$

The vectors of conservation variables and fluxes are given by

$$\boldsymbol{U} = \rho \begin{Bmatrix} 1 \\ u_1 \\ u_2 \\ e \end{Bmatrix} \qquad \boldsymbol{F}_i^v = \begin{Bmatrix} 0 \\ \tau_{1i} \\ \tau_{2i} \\ \tau_{ij}u_j \end{Bmatrix}$$

$$\boldsymbol{F}_i^a = u_i + p \begin{Bmatrix} 0 \\ \delta_{1i} \\ \delta_{2i} \\ u_i \end{Bmatrix} \qquad \boldsymbol{F}_i^h = \begin{Bmatrix} 0 \\ 0 \\ 0 \\ -q_i \end{Bmatrix} \tag{9}$$

where ρ is the density, u_i the velocity components in the coordinate directions, p the thermodynamic pressure, e the total energy, q_i the heat fluxes, τ_{ij} the viscous stress components, and δ_{ij} the Kronecker delta. The shear stresses and heat fluxes are given by

$$\tau_{ij} = \lambda u_{k,k}\delta_{ij} + \mu(u_{i,j} + u_{j,i}) \tag{10a}$$

$$q_i = -kT_{,i} \tag{10b}$$

where μ and λ are the coefficients of viscosity, k the thermal conductivity, and T the temperature. Other constitutive relations employed include

$$e = C_v T + \frac{(u^2 + v^2)}{2} \tag{11a}$$

$$p = \rho RT \tag{11b}$$

where C_v is the specific heat at constant volume and R the gas constant. The coefficients of viscosity are related by Stokes hypothesis

$$\lambda = -\frac{2}{3}\mu \tag{12}$$

and μ is assumed a function of temperature obtained by Sutherland's law. The thermal conductivity is computed from the Prandtl number Pr, which is assumed constant along with constant specific heats. Equation (7) is solved subject to proper initial and boundary conditions, which include 1) specification

of conservation variables on the inflow plane, 2) imposition of no-slip conditions and specified temperatures on aerodynamic surfaces, and 3) outflow surface integrals provided by the finite element formulation.

Galerkin-Runge-Kutta Algorithm

The system of conservation laws shown in Eq. (7) can be written as,

$$\boldsymbol{U}_{,t} = -\boldsymbol{E}_{i,i} \tag{13}$$

Application of the method of weighted residuals results in the finite element equations,

$$\int_A [N]\left\{\frac{\partial \boldsymbol{U}}{\partial t}\right\} dA = -\int_A [N]\boldsymbol{E}_{i,i}\, dA \tag{14}$$

where $[N]$ is the element weighting and interpolation function and A the domain of interest. Integrating by parts on the right side yields,

$$[M]\left\{\frac{\partial \boldsymbol{U}}{\partial t}\right\} = \int_A \{N_{,i}\}[N]\, dA\{\boldsymbol{E}_i\} - \int_S \{N\}[N]\, ds[\lambda_i \boldsymbol{E}_{is}] \tag{15}$$

where the fluxes $\boldsymbol{E}_i$ are interpolated the same way as the conservation variables.

Spatial derivatives of velocities and temperature in the coordinate directions are computed for each element by using the symbolic manipulation program MACSYMA.[12] These gradients are then multiplied by appropriate values of viscosity and thermal conductivity to obtain element nodal values of the viscous and heat flux vectors. The element matrices in Eq. (15) can also be evaluated in closed form, greatly reducing computational costs.

The time-marching scheme is similar to the multistep time integration scheme, which appears in Ref. 10, and can be written as,

$$\boldsymbol{U}_j^{(k)} = \boldsymbol{U}_j^n + c^k\left[\frac{\Delta t_j}{M_{jj}} R_j(\boldsymbol{U}^{k-1}) + \boldsymbol{D}\right] \quad k = 1,4 \tag{16a}$$

$$\boldsymbol{U}_j^{n+1} = \boldsymbol{U}_j^{(4)} \tag{16b}$$

where the dissipation operator D can be written as,

$$\boldsymbol{D} = \boldsymbol{D}_2^n + \boldsymbol{D}_4^n \tag{17}$$

and $\boldsymbol{D}_2$ and $\boldsymbol{D}_4$ are second- and fourth-difference dissipation terms, which may be frozen for each time step. Details of the dissipation operators appear in Ref. 10.

Calculation of Wall Coefficients

Heat transfer, skin friction, and pressure coefficients are essential for design considerations since they provide a direct measure of the severity of aerodynamic loads on flight surfaces. The heat transfer and shear stress coefficients are related to the gradients of temperature and fluid velocity at the surface. With a structured computational grid, it is possible to calculate derivatives at the wall by simple differencing techniques and obtain results of desired accuracy. For completely unstructured finite element meshes, the calculation of wall derivatives by differencing is rather complicated. Computation of heat fluxes and shear stresses at the wall is possible in the finite element context by using the consistent calculations. These calculations, introduced in Ref. 13, use Eq. (15) as the basis for computing wall coefficients.

The finite element equations, Eq. (15), can be written as

$$\frac{\partial \boldsymbol{U}}{\partial t} = \int_A \{N_{,i}\}[N]\, dA\{\boldsymbol{E}_i\} - \int_S \{N\}[N]\, ds[\lambda_i \boldsymbol{E}_{is}] \tag{18}$$

At steady state, the transient terms approach zero, implying

$$\int_s \{N\}[N]\, ds[\lambda_i \boldsymbol{E}_{is}] = \int_A \{N_{,i}\}[N]\, dA\{\boldsymbol{E}_i\} \tag{19}$$

Surface Stresses

The x- and y-momentum equations for elements on the surface reduces to,

$$\int_s \{N\}[N]\, ds\{T_x\} = \{R_x\} \tag{20a}$$

$$\int_s \{N\}[N]\, ds\{T_y\} = \{R_y\} \tag{20b}$$

where T_x and T_y are the surface tractions and R_x and R_y the residuals for an element. These equations are assembled for all of the elements that lie on the surface. Diagonalizing the matrices defined by the surface integrals in Eq. (20) yields an explicit procedure for obtaining nodal values for the surface tractions. The surface tractions are related to the stress tensor by the relation,

$$\begin{Bmatrix} T_x \\ T_y \end{Bmatrix} = \begin{bmatrix} \tau_{xx} & \tau_{xy} \\ \tau_{yx} & \tau_{yy} \end{bmatrix} \begin{Bmatrix} n_x \\ n_y \end{Bmatrix} \tag{21}$$

where τ_{ij} are components of the stress tensor, and n_x and n_y are components of the unit vector $\boldsymbol{n}$, normal to the surface. The wall shearing stress is then given by,

$$\tau_w = T_n n_x - T_x n_y \tag{22}$$

Surface Heat Flux

At steady state, the energy equation for elements that lie on the surface can be written as,

$$\int_s \{N\}[N]\, ds\{q_n\} = \{R_n\} \tag{23}$$

where q_n is the nodal heat flux for an element. Diagonalizing the coefficient matrix and assembling the element equations yields nodal values of the heat flux on the surface.

The coefficients of heat transfer C_H, skin friction C_f, and pressure C_p are computed from the relations,

$$C_H = \frac{q_w}{\rho_\infty u_\infty\{[e + (p/\rho) + (u^2/2)]_\infty - [e + (p/\rho)_w\}} \tag{24a}$$

$$C_f = \frac{\tau_w}{\rho_\infty u_\infty^2} \tag{24b}$$

$$C_p = \frac{p_w}{(\rho_\infty u_\infty^2)/2} \tag{24c}$$

where p_∞, ρ_∞, and u_∞ are freestream values, and p_w is the wall pressure.

Computational Results

The ability of the adaptive finite element procedure to predict heating rates and pressure loads for high-speed flows is illustrated by modeling the laminar hypersonic flow over a ramp. This problem has special interest due to its application in the design of control surfaces for hypersonic vehicles.

The use of a second-order accurate finite difference scheme for Mach 14.1 corner flows over different wedge angles for obtaining skin friction and heating rates appears in Ref. 14. References 15 and 16 also detail flow characteristics for flows of Mach numbers 14.1 and 18.9 using MacCormack's[17] method. In these efforts, skin friction and heat transfer coefficients were compared to experimental results of Holden.[18] The present effort will model Mach 11.68 laminar flow over the wedge

angle of 15 deg and compare with Holden's experimental results to gauge the accuracy of the finite element calculations.

Flow Description

The problem is illustrated schematically in Fig. 2. Inflow at Mach 11.68 interacts with a leading edge producing a shock due to the boundary-layer displacement effect. The boundary layer separates due to the adverse pressure gradient generated by the ramp resulting in recirculation near the corner. The separated boundary layer then reattaches downstream of the corner with the surface pressure rising through the separated and reattachment regions. The compression fan generated in the separation zone eventually coalesces downstream to form the induced shock. This shock interacts with the leading-edge shock to produce a resultant shock, an expansion fan, and a shear layer or slip line.

The interaction between the inner viscous shear layer and the outer inviscid flow can be categorized based on the nature of coupling. At the leading edge of the plate, the induced shock and the boundary layer are essentially of the same order, and the effects of the interaction can be reasonably predicted by various interaction theories. At the corner separation results upstream of the induced shock due to the coupling between the shock and the thickening of the boundary layer due to compression. This type of interaction necessitates the solution of the full Navier-Stokes equations.

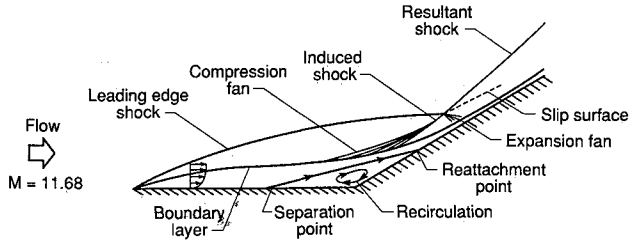

Fig. 2 Hypersonic flow over a 15-deg ramp.

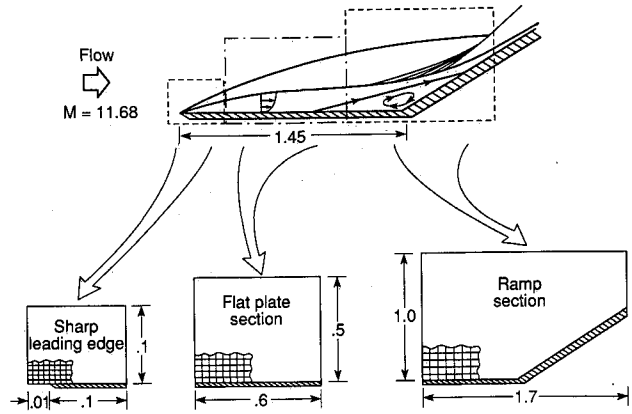

Fig. 3 Subdivision of hypersonic flow domain: sharp leading edge, flat plate, and ramp.

Strong Interaction Theory

Near the sharp leading edge, the displacement thickness increases from zero and the flow turning outside of the boundary layer causes compression and a leading-edge shock. The strength of the shock depends on the incident Mach number and has a strong effect on the growth of the boundary layer at the leading edge. Near the leading edge, the pressure at the edge of the boundary layer is very high compared to the freestream pressure marking the region of strong interaction. Downstream of the leading edge the interaction between the inviscid and viscous flow weakens and the wall pressure expands to freestream.

From laminar boundary layer theory, the appropriate similarity parameter for the shock boundary-layer interaction is the Lees-Probstein parameter X given by

$$X = \frac{M_\infty^3 \sqrt{C}}{\sqrt{Re_x}} \tag{25}$$

where C is the Chapman-Rubesin compressibility parameter, M_∞ the freestream Mach number, and Re_x the local Reynolds number. The effects of the coupling between the leading-edge shock and the boundary layer have been predicted by various strong[19,20] and weak[21] interaction theories. The complete interaction theory of Bertram and Blackstock[22] unifies the strong and weak interaction theories by bridging their limits of applicability. Assumptions used in the development of these interaction theories include the following: 1) the flow is hypersonic ($M_\infty >> 1$), 2) no gas dissociation, 3) Prandtl number constant, 4) vorticity effects due to the curved leading-edge shock are negligible, and 5) pressure distribution is assumed to vary exponentially with distance from the leading edge. The interaction theory relates the surface pressure to the interaction parameter X as follows,

$$\frac{P}{P_\infty} = 0.83 + \frac{3}{4}\sqrt{\frac{\lambda(\lambda+1)}{2}}\,GX \tag{26}$$

where G is the growth factor defined as,

$$G = 1.648\,\frac{(\lambda-1)}{2}\left[\frac{T_w}{T_{aw}} + 0.352\right] \tag{27}$$

and T_{aw} is the adiabatic wall temperature given by

$$T_{aw} = T_\infty\left[1 + \frac{(\lambda-1)}{2}\sqrt{Pr}\,M_\infty^2\right] \tag{28}$$

for laminar flows. The variation of heat transfer coefficient with surface temperature in the strong interaction region is

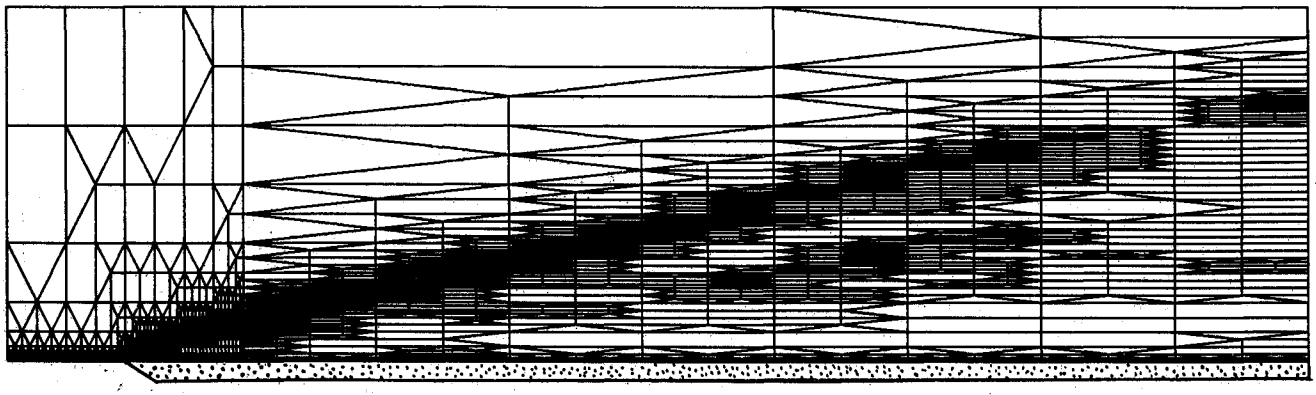

Fig. 4 Finite element mesh for sharp leading edge.

tabulated by Li and Nagamatsu.[19] For $\lambda = 1.4$, the variation of C_H with wall temperature T_w is given by

$$C_H \left[\frac{Re_x}{X}\right]^{0.5} = C_1 \tag{29}$$

where the constant C_1 depends on T_w and the ratio of specific heats and is obtained from Ref. 23.

Experimental Results

The experimental studies used for validation of the finite element approach were conducted in the Calspan 48-in. shock tunnel. Skin friction transducers, thin-film resistance thermometers, and pressure transducers were mounted at suitable locations to obtain skin friction, heat transfer, and surface pressure measurements. Details of the experiments are described by Holden.[18]

The flow parameters used in the numerical computations correspond to the nominal test conditions for hypersonic flow over a ramp presented in Ref. 18. The experimental data used for comparison with finite element results correspond to tunnel run 21. Flow conditions are given as,

Nominal	Run 21
M_∞ = 11.68	M_∞ = 11.64
Re_∞ = 1.714E + 05/ft	Re_∞ = 1.644E + 05/ft
T_{res} = 2989 R	T_{res} = 3105 R
P_d = 0.3589 psia	P_d = 0.369 psia

The measurements[24] in the Calspan shock tunnel yield heating rates, surface pressures, and skin friction at various locations on the control surface. The coefficients of pressure and skin friction are obtained by dividing experimental values by the freestream dynamic pressure. The coefficient of heat transfer is obtained from the heat flux at the wall by the relation,

$$C_H = \frac{q_w}{\rho_\infty u_\infty \gamma C_v [T_{res} - T_w]} \tag{30}$$

where the wall temperature T_w assumed to be the same for both runs is obtained from Ref. 18, and the specific heat is assumed constant.

Computational Strategy

The hypersonic flow over a ramp results in inviscid-viscous interactions that have distinctly different character in various regions of the domain. Near the leading edge, the mesh needs to be well refined and nearly uniform to capture gradients in both the streamwise and normal directions. Away from the leading edge, the flow includes the growth of the boundary layer and graded mesh spacings at the surface in the normal direction are needed. At the corner, the coupling between the inviscid and viscous regions necessitates detailed refinement to capture the separated and attached regions of flow.

The analysis divided the flow domain into three regions. The three regions are shown in Fig. 3 and are categorized as 1) the sharp leading-edge section, 2) the flat plate section, and 3) the ramp section.

Sharp Leading Edge

The mesh used for modeling the sharp leading edge section is shown in Fig. 4 and contains 4957 nodes and 5063 elements. A closer view of the mesh at the leading edge is shown in Fig. 5 and illustrates the smallest elements being located in a band through which the leading-edge shock passes. Density contours in Fig. 6 show good definition of the leading-edge shock and smooth variation of density within the boundary layer. At the leading edge, the boundary-layer displacement effect causes the density at the wall to increase by an order of magnitude and then to drop off quite rapidly away from the leading edge.

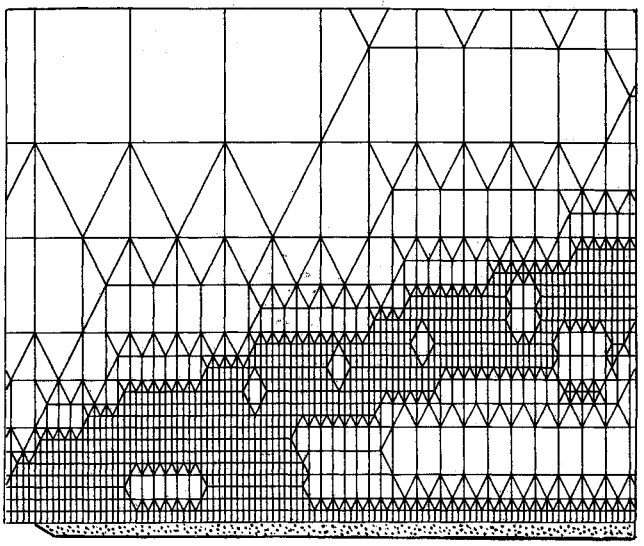

Fig. 5 Detail of mesh near the leading edge.

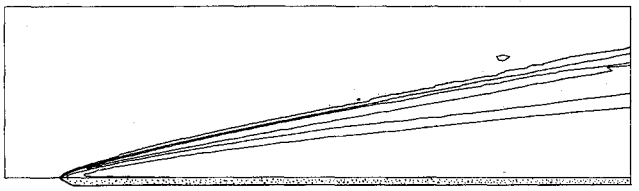

Fig. 6 Density contours for sharp leading edge.

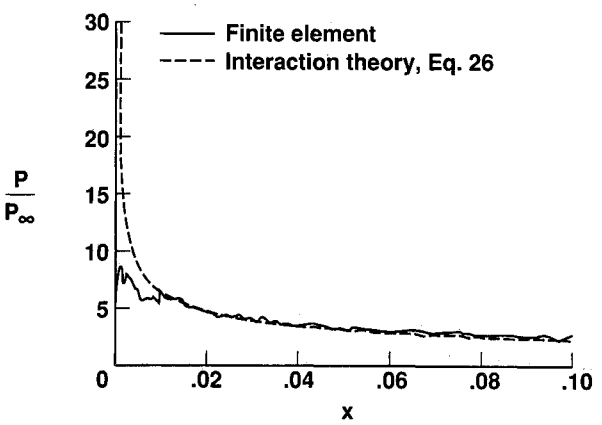

Fig. 7 Comparison of pressure coefficients for the sharp leading edge.

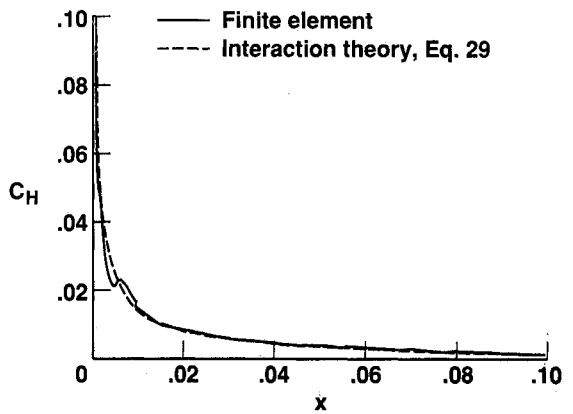

Fig. 8 Comparison of heat transfer coefficients for the sharp leading edge.

The surface pressure and heat transfer coefficient obtained from this analysis are compared to predictions by the interaction theories in Figs. 7 and 8. The results compare favorably, especially the heat transfer coefficient. The maximum deviation in pressure levels is seen to be near the leading edge and indicates the need for further mesh refinement at this location.

Flat Plate Section

Profiles of the conservation variables obtained at the exit of the leading-edge section are used as inflow conditions to the flat plate section. A comparison of the density profiles at the outflow of the leading edge and at inflow to the flat plate section in Fig. 9 indicates the adequacy of nodal distribution in the normal direction.

The finite element mesh used to model the flat plate region contains 7757 and 7875 elements and is shown in Fig. 10. In addition to refinement and derefinement, each element at the wall was divided up into 10 subelements according to Eqs. (5). The grid parameter β was set to be 1.02 and the subdivision yields elements with aspect ratios over 200 at the wall. Density contours on this mesh appear in Fig. 11. Elements are seen to be clustered at the shock, and the mesh density is adequate to detail the growth of the boundary layer along the plate. As with the leading-edge section, profiles on the exit plane ($x = 0.7$) of the flat plate section are used to define the inflow boundary of the ramp section.

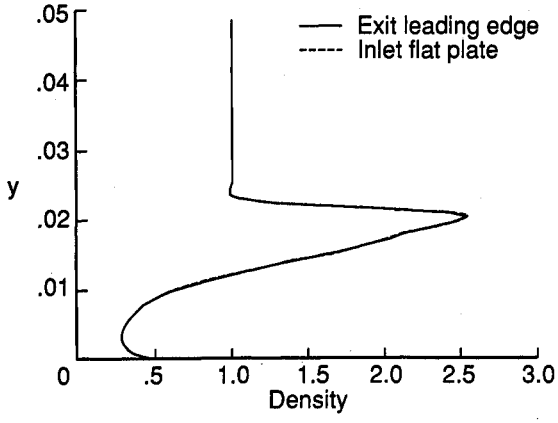

Fig. 9 Density profiles at exit of the leading edge and inflow to the flat plate section.

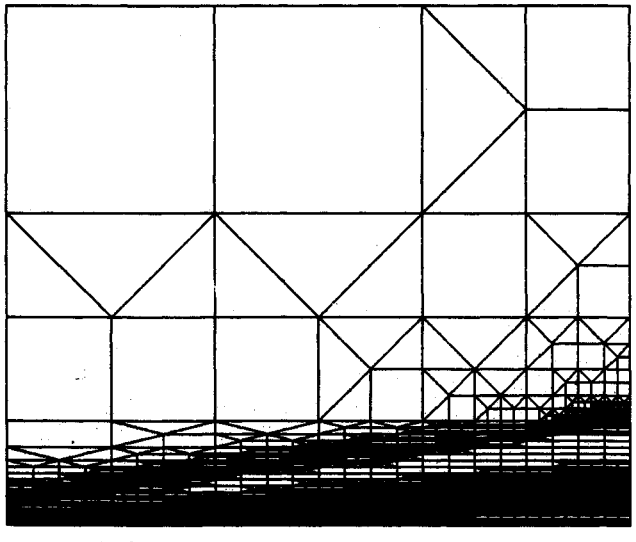

Fig. 10 Finite element mesh for flat plate section.

Ramp Section

The finite element mesh used for the ramp section is shown in Fig. 12. On an initial crude mesh, each element at the wall was divided into 10 subelements with a stretching factor of 1.03. The mesh was obtained after three levels of refinement and contains 6763 nodes and 6880 elements. The ability of the adaptive refinement procedure to locate regions of high gradients is exhibited by taking a closer look at the mesh in the ramp corner. The mesh in Fig. 13 and density contours

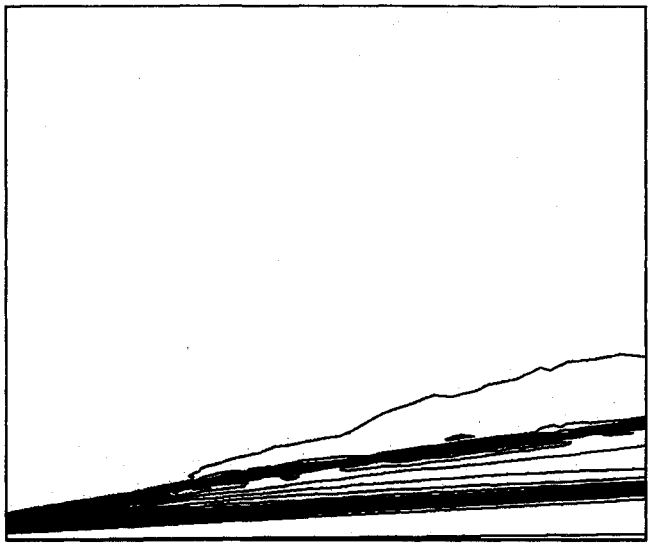

Fig. 11 Density contours for flat plate section.

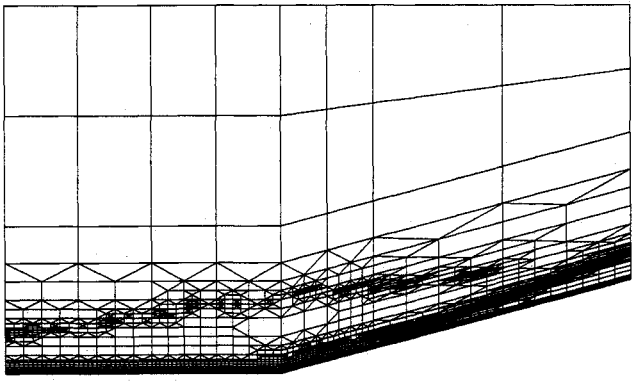

Fig. 12 Finite element mesh for ramp section.

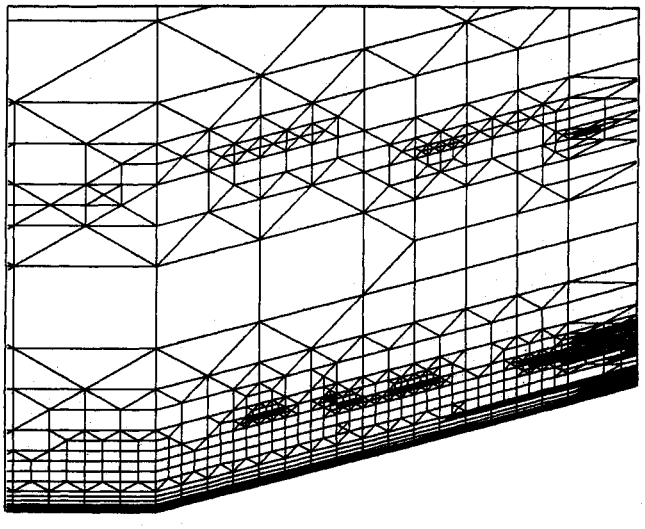

Fig. 13 Mesh detail at the corner of the ramp.

on this mesh in Fig. 14 illustrate capture of the leading-edge shock and compression of flow that results in the induced shock downstream of this region. The fine mesh at the surface is needed to model separation and subsequent reattachment of the boundary layer in the vicinity of the corner. Explicit dissipation terms for elements that are located close to the surface were "zeroed out" to ensure accurate computation of surface quantities.

Details of the flowfield, especially the coupling between the inviscid and viscous regions of flow, are best described by profiles of select variables at specified axial locations. Fig. 15 indicates the x stations where variation in the y direction of flow variables are plotted. Locations indicated by A, B, C, and D are used to describe flow details in the domain up to the corner, whereas locations E–H detail flow characteristics up the ramp.

The distribution of pressure normal to the surface at locations A–D is shown in Fig. 16. As the flow moves from the inlet toward the corner, the presence of the adverse pressure gradient due to the ramp is clearly seen. Fluid in the vicinity of the corner cannot overcome the effects of the pressure gradient as well as the skin friction at the wall and flow separation results. The boundary-layer separation is seen in Fig. 17 by the reversal in flow direction of u-velocity profiles.

Characteristics of the flow up the ramp are described by the distributions at locations E–H. Pressure profiles at E, F, and G in Fig. 18 indicate the strengthening of the induced shock and the change in location of the leading-edge shock relative to the surface. The distribution of pressure at exit of the ramp (location H) shows the resultant shock that is derived from the interaction of the leading-edge shock with the induced shock. A weak expansion fan also results from this interaction, the effect of which is seen by the small drop in surface pressures at location H relative to that at G. Thinning of the boundary layer as the flow moves up the ramp is seen in Fig. 19, which shows u-velocity profiles at various x stations. The presence of the recirculation is seen by the flow

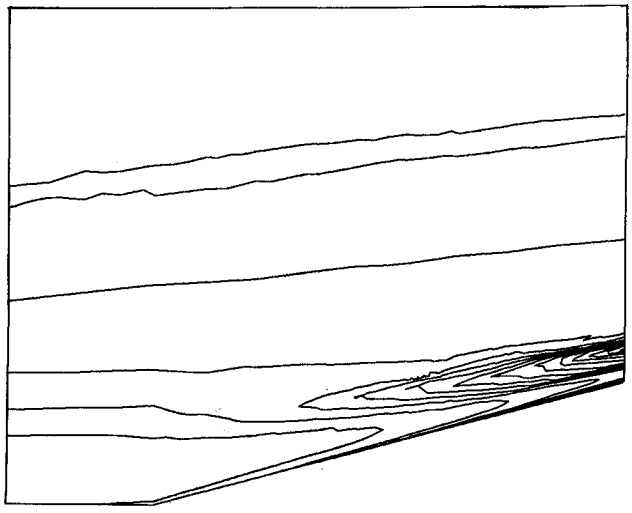

Fig. 14 Density contours at corner of the ramp.

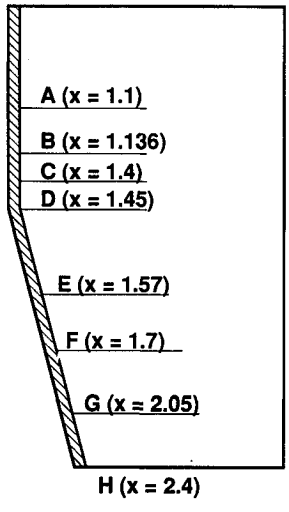

Fig. 15 Locations of profile stations along the ramp.

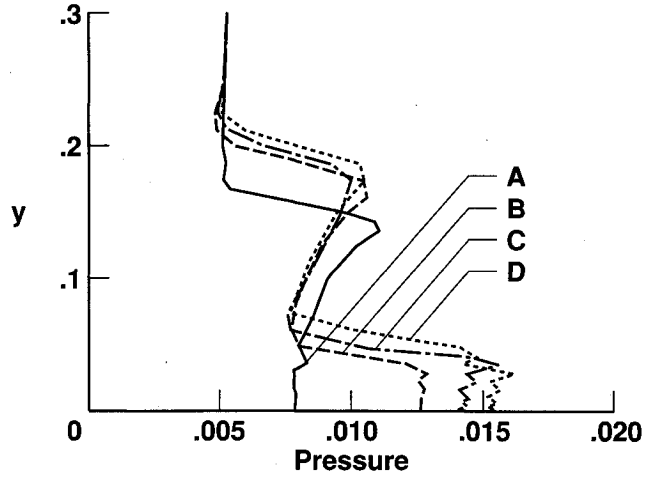

Fig. 16 Pressure distribution at locations on flat portion of ramp.

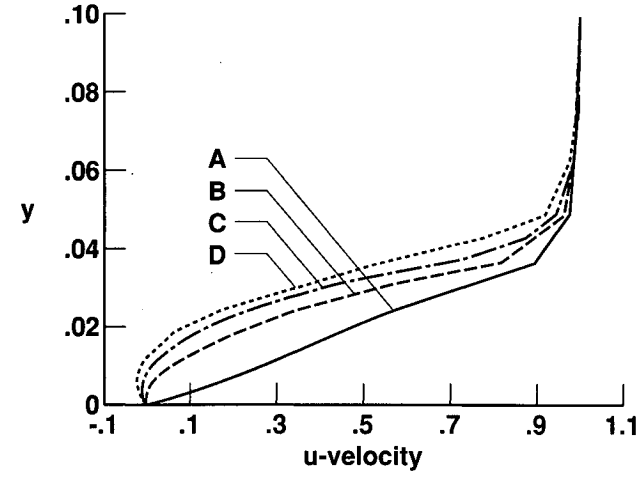

Fig. 17 Velocity profiles at locations on flat portion of ramp.

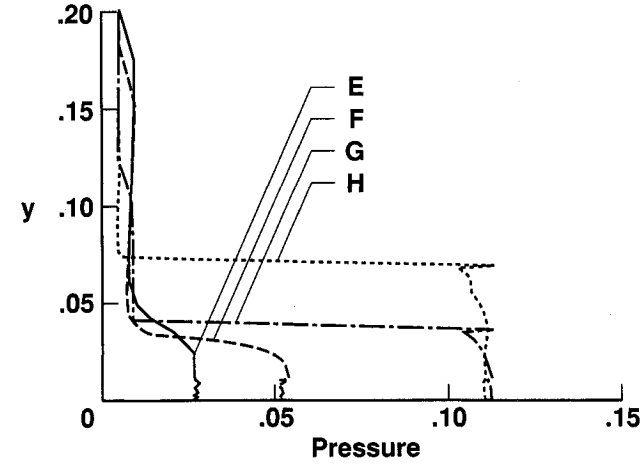

Fig. 18 Pressure profiles at locations up the ramp.

reversal close to the surface at station E. At the exit from the ramp section, the boundary-layer profile is fully developed, and downstream of this region the interaction between the inviscid and viscous regions of the flowfield is negligible.

Heat flux, skin friction, and pressure coefficients for the ramp surface obtained from the finite element approach are compared to experimental results of Holden.[24] Figure 20 compares the finite element predictions for heat transfer coefficient to those obtained from experiment. The heat transfer coefficients match quite well at the separation and reattachment regions and the values of the peak heating rate are in excellent agreement. The main discrepancies are the location of the peak heating rate, which, for the analysis, is shifted to the left and a steeper drop in heating rates downstream of this location.

Skin friction coefficients calculated from the finite element approach are compared to those measured in tunnel run 21 in Fig. 21. Levels of the skin friction coefficient compare well with the experimental data for regions unaffected by the recirculation, whereas the size of the recirculation region is underpredicted by the finite element approach. Experimental runs measure flow separation at around $x = 15$ in., whereas the finite element predictions locate separation at $x = 16$ in. The location of the reattachment point from run 21 is $x = 20.3$ in. and the finite element procedure locates this point at $x = 19.3$ in.

A comparison of surface pressure coefficients using the finite element approach with data from experimental run 21 appears in Fig. 22. Pressure levels predicted by the analysis is seen to be lower at the inflow and recirculation regions and the pressure rise up the ramp is much more rapid. The experimental data shows the pressure peak near the exit, whereas

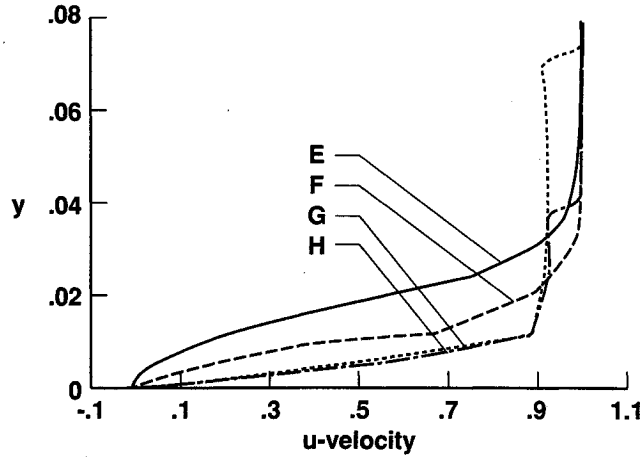

Fig. 19 Velocity profiles at locations up the ramp.

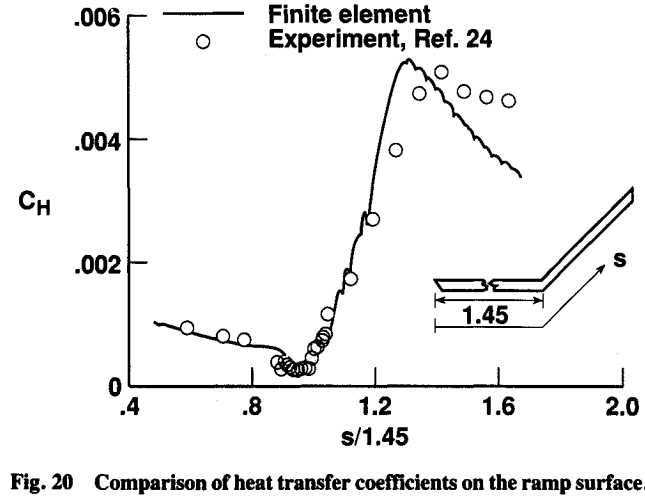

Fig. 20 Comparison of heat transfer coefficients on the ramp surface.

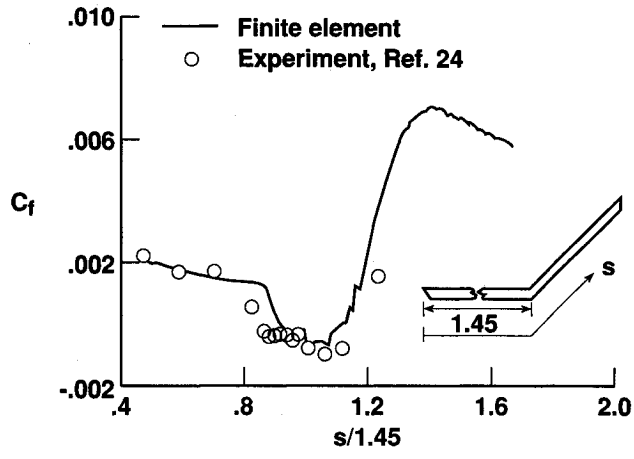

Fig. 21 Comparison of skin friction coefficients on ramp surface.

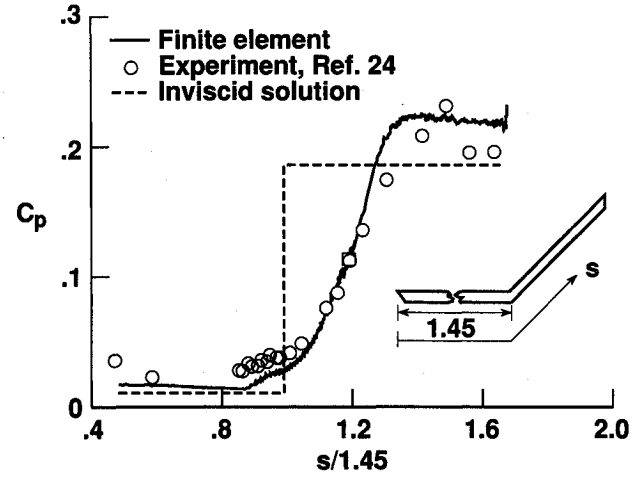

Fig. 22 Comparison of surface pressure coefficients on ramp surface.

the finite element approach indicates a gradual downward trend. This implies that the interaction between the leading-edge shock and induced shock is stronger than that predicted by the finite element approach. The pressure rise for Mach 11.7 inviscid flow over a 15-deg ramp is about 17.5 and the finite element analysis yields a peak pressure rise of over 22.

Concluding Remarks

An adaptive finite element procedure that uses both triangles and quadrilateral elements is coupled with a multistep Galerkin-Runge-Kutta algorithm to model laminar hypersonic compressible flows. The finite element mesh is adapted in regions of high gradients by the use of inviscid and viscous refinement indicators. Layers of structured quadrilateral elements at the wall are included for better representation of the boundary layer.

The ability of the adaptive finite element procedure to predict heating rates and pressure loads on flow surfaces is demonstrated by modeling the Mach 11.7 flow over a ramp. To ensure adequate resolution of complex flow features, the flow domain is split up into three subregions: 1) the sharp leading edge, 2) the flat plate region, and 3) the ramp section.

The accuracy of the finite element solution at the sharp leading-edge section is evaluated by comparison with predictions of strong interaction theories. The complete theory of Bertram and Blackstock yields estimates for surface pressure distributions, whereas the heat transfer coefficient is obtained from the strong interaction theory of Li and Nagamatsu. Good correlations between the finite element predictions and the

strong interaction theories are obtained for the leading-edge section.

The finite element mesh for the ramp section captures the physics of the complicated viscous-inviscid interactions at the corner. The effect of the leading-edge shock on the surface is seen by the peak in heating rates near the exit section of the ramp. Surface coefficients of heat transfer, skin friction, and pressure obtained from the finite element calculations generally compare well with the experimental measurements of Holden with some exceptions.

The study highlights some of the complexities involved in modeling compressible viscous flow problems, especially, high-speed flows with strong shock boundary-layer interactions. The physics of the flow as well as surface coefficients obtained from the adaptive finite element approach compare favorably with theoretical and experimental data. This trend is encouraging and indicates that the adaptive procedures have potential for accurate aerothermal load predictions in high-speed flows.

Acknowledgment

The research of R. Ramakrishnan and E. A. Thornton was supported by research Grant NSG-1321 through the Aerothermal Loads Branch at NASA Langley Research Center.

References

[1]Bey, K. S., Thornton, E. A., Dechaumphai, P., and Ramakrishnan, R., "A New Finite Element Approach for Prediction of Aerothermal Loads-Progress in Inviscid Flow Computations," AIAA Paper 85-1533, July 1985.

[2]Thareja, R. R., Stewart, J. R., Hassan, O., Morgan, K., and Peraire, J., "A Point Implicit Unstructured Grid Solver for the Euler and Navier-Stokes Equations," AIAA Paper 88-0036, January 1988.

[3]Thornton, E. A., Ramakrishnan, R., and Dechaumphai, P., "A Finite Element Approach for Solution of the 3D Euler Equations," AIAA Paper 86-0106, January 1986.

[4]Dechaumphai, P., Thornton, E. A., and Wieting, A. R., "Flow-Thermal-Structural Study of Aerodynamically Heated Leading Edges," *Journal of Spacecraft and Rockets*, Vol. 26, No. 4, 1989, pp. 201–209.

[5]Zienkiewicz, O. C., Lohner, R., and Morgan, K. "High Speed Inviscid Compressible Flow by the Finite Element Method," *Mathematics of Finite Elements and Approximations*, edited by J. R. Whiteman, Academic, 1985, pp. 1–26.

[6]Stewart, J. R., Thareja, R. R., Wieting, A. R., and Morgan, K., "Application of Finite Element and Remeshing Technique to Shock Interference on a Cylindrical Leading Edge," AIAA Paper 88-0368, January 1988.

[7]Lohner, R., "The Efficient Simulation of Strong Unsteady Flows by the Finite Element Method," AIAA Paper 87-0555, January 1987.

[8]Oden, J. T., Demkowicz, L., Strouboulis, T., and Devloo, P., "Adaptive Methods for Problems in Solid and Fluid Mechanics," *Adaptive Methods and Error Refinement in Finite Element Computation*, edited by I. Babuska, O. C. Zienkiewicz, J. P. de S. R. Gago, and A. de Oliveira, Wiley, London, England, UK, 1986.

[9]Peraire, J., Vahdati, M., Morgan, K., and Zienkiewicz, O. C., "Adaptive Remeshing for Compressible Flow Computations," *Journal of Computational Physics*, Vol. 72, No. 2, 1987, pp. 449–466.

[10]Ramakrishnan, R., Bey, K. S., and Thornton, E. A., "An Adaptive Quadrilateral and Triangular Finite Element Scheme for Compressible Flows," *AIAA Journal*, Vol. 14, No. 1, 1990, pp. 51–59.

[11]Roberts, G. O., "Computational Methods for Boundary Layer Problems," *Proceedings of the Second International Conference in Numerical Methods in Fluid Dynamics*, Lecture Notes in Physics, Vol. 8, Springer-Verlag, NY, pp. 171–177.

[12]The Mathlab Group, "*MACSYMA Reference Manual*," Version 9, The Mathlab Group Laboratory for Computer Science, Massachusetts Inst. of Technology, Cambridge, MA, Dec. 1977.

[13]Thornton, E. A., Dechaumphai, P., and Vemaganti, G., "A Finite Element Approach for Prediction of Aerothermal Loads," AIAA Paper 86-1050, May 1986.

[14]Hung, D. M., and MacCormack, R. W., "Numerical Solutions of Supersonic and Hypersonic Laminar Compression Corner Flows," *AIAA Journal*, Vol. 14, No. 4, 1976, pp. 475–481.

[15]Ray, R., Erdos, J., and Pulsonetti, M. V., "Hypersonic Laminar Strong Interaction Theory and Experiment Revisited Using a Navier-Stokes Code," AIAA Paper 87-1191, June 1987.

[16]Power, G. D., and Barber, T. J., "Analysis of Complex Hypersonic Flows with Strong Viscous/Inviscid Interaction," *AIAA Journal*, Vol. 26, No. 7, 1988, pp. 832–840.

[17]MacCormack, R. W., "The Effect of Viscosity in Hypervelocity Impact Cratering," AIAA Paper 69-354, May 1969.

[18]Holden, M. S., "A Study of Flow Separation in Regions of Shock Wave-Boundary Layer Interaction in Hypersonic Flow," AIAA Paper 78-1169, July 1978.

[19]Li, T. Y., and Nagamatsu, H. T., "Similar Solutions of Compressible Boundary Layer Equations," *Journal of Aeronautical Sciences*, Vol. 20, No. 5, 1953, pp. 653–655.

[20]Lees, L., and Probstein, R. F., "Hypersonic Viscous Flow over a Flat Plate," Aeronautical Engineering Laboratory, Princeton Univ., Princeton, NJ Rept. 195, April 1952.

[21]Hayes, W. D., and Probstein, R. F., *Hypersonic Flow Theory*, Academic, New York, 1959, pp. 341–353.

[22]Bertram, M. H., and Blackstock, T. A., "Some Simple Solutions to the Problem of Predicting Boundary-Layer Self-Induced Pressure," NASA TN D-798, April 1961.

[23]Dorrance, W. H., *Viscous Hypersonic Flow*, McGraw-Hill, New York, 1962, pp. 154–157.

[24]Calspan Corporation, "Laminar Flow Data Base," Aug. 1987.